Triply Periodic Minimal Surfaces Casing Treatment on an Axial Flow Fan: A Computational Aeroacoustic Study

Mostafa Mozafari[1], Mehran Masdari[2], Mojtaba Tahani[3]

1&3 College of Interdisciplinary Science and Technology, University of Tehran, Northern Kargar, 1439557131 Tehran, Iran.
2 School of Science & Technology, City St George's, University of London, Northampton Square, London, EC1V 0HB, United Kingdom

Corresponding author: mehran.masdari@citystgeorges.ac.uk

Abstract

Axial flow fans are essential for cooling processes in various industrial settings, making noise reduction a vital factor. Initial studies indicate that adding a porous structure to the fan casing can effectively reduce noise caused by tip leakage vortices. Expanding on this idea, a porous casing based on Triply Periodic Minimal Surfaces (TPMS) was used to assess the fan's aeroacoustic performance. This study introduces the first application of TPMS casings for axial fan tip-leakage noise control. A thorough experimental and numerical analysis was carried out to investigate the aerodynamic properties and identify the mechanisms behind noise reduction. The findings show that the porous casing notably diminishes the strength and size of the tip leakage vortex while also decreasing turbulence intensity near the casing walls. Additionally, the analysis indicates that the degree of noise reduction depends on both the porosity percentage and unit cell size. A diamond TPMS structure with 55% porosity and a unit cell size of 6 mm provides an optimal configuration, enhancing viscous damping and sound energy absorption at low frequencies. This well-designed TPMS structure can effectively reduce both blade passing frequency and turbulence interaction noise, achieving an overall noise reduction of up to 10 dB.

Keywords: Noise reduction, Acoustics, Computational fluid dynamics (CFD), Porous Casing, Lattice-Boltzmann method (LBM), Large Eddy Simulation (LES).

Nomenclatures

TPMS	Triply Periodic Minimal Surfaces	DAQ	Data acquisition
AFF	Axial Flow Fan	3D	Three Dimensional
BPF	Blade Passing Frequency	SPL	Sound Pressure Level
dB	Decibel	OASPL	Overall Sound Pressure Level
p	porosity	w	unit cell size
P	acoustic power	ONR	Overall Noise Reduction
IL	Insertion Loss	rpm	revolutions per minute

1- Introduction

Axial flow fans (AFF) are widely used in the fields of electronic equipment, air conditioning, and several other applications [1]. As users demand quieter cooling, the need to enhance the acoustic

performance of an axial fan has gained prominence. One of the major sources of noise pollution is axial fans, and considerable efforts have been made to reduce their acoustic emissions [2]. The well-known kind of fan noise due to fluid flow at the tip is tip leakage flow, which is especially important for small axial fans. This is because unsteady tip-leakage flows induce pressure fluctuations on the blade surfaces, producing tip clearance noise. Moreover, coupling of the tip vortices with downstream stator vanes can increase the overall noise levels [3]. The narrow-band noise in the clearance region between the fan and the shroud is due to the secondary flow near the blade-shroud junction. In residential, commercial, and industrial, reducing fan noise is a must to create quiet neutral environments. Further, acoustic performance has emerged as a primary differentiator among manufacturers in the intensely competitive consumer cooling products market [4].

Engineers employ porous casings, micro-perforated panels (MPPs), and fibrous materials to mitigate noise from radial and tip leakage flows in axial flow fans. Although each type has its specific advantages for noise cancellation, they affect airflow in various ways. Porous casings (open-cell metal foam) are used to reduce tip leakage vortices by equalizing pressure on the two sides of the blade (pressure and suction). This porous surface makes the leakage flow pass through its form, disturbing the tip flow field. While it slightly handles aerodynamics, it also works to serve as a pressure release boundary to minimize near-field noise and reduce sound propagation at the far field. An MPP liner consists of a thin panel, which has little malfunctioning air cavity and perforations. MPPs, as opposed to other porous materials, hardly react with bulk and absorption. The panels can be laid on top of the fan rotor to dampen noise levels at different flow rates. Moreover, MPP treatments modify the airflow around the blade tips, which lessens the contribution of wake-rotor and tip-vortex interactions on noise. Conventional fibrous materials (e.g., fiberglass) are extremely effective at sound absorbing, but may not be suited for demanding environments where dust, moisture, and/or temperature changes might lead to a decline in performance. Such noise reduction methods provide several advantages that allow manufacturers to tailor solutions specific to the performance needs and surrounding conditions [3, 5, 6]. Several studies have investigated axial fan noise reduction, particularly the radial and tip leakage noise. Sutliff and Jones investigated using foam-metal liners to reduce noise in low-speed fans and showed that locating foam-metal liners near the rotor alters acoustic near-field and suppresses noise-generation mechanisms. [7]. However, since foam-metal liners are only effective if the fan tip speed is maintained below sonic levels, large reduction factors in his work could be achieved, without any significant performance loss [8]. Other studies have shown that if you pop MPP liners on the front rotor of contra-rotating fans, noise is effectively reduced. The stiffness of the cavity is reduced per the enlargement of the cavity behind the MPP liner to achieve improved noise attenuation. This configuration was effective in attenuating rotor-alone tones but was not with a blunt front treatment [9]. Open-cell metal foam casings have been shown to reduce noise by attenuating the tip leakage vortex and pushing back stall inception. This is accomplished by decreasing the pressure difference across the pressure and suction sides of the blade and by promoting momentum transfer across the fluid-pore interface. Under stalled conditions, it has been demonstrated that it can reduce sound by as much as 10 dBA with this method [3]. Additionally, researchers have shown that perforated surfaces in the axial fan shroud can break up coherent flow structures in the clearance region and spanwise counter-rotating vortices at the trailing edge, thus

reducing radiated noise at the most critical blade pass frequency while maintaining aerodynamic performance [4]. Sun et al. related research on foam-metal casing treatments for axial flow compressors. Their results are consistent with previous research, indicating that porous casings add extra damping, which restricts noise diffusion and dampens early disturbances [10, 11].

These investigations aim to study different kinds of materials and methods to reduce the radial and tip leakage noise of axial flow fans. Conventional porous treatments offer some tonal noise reduction but fall short in broadband and low-frequency performance. Micro-perforated plates can even amplify noise above 3 kHz due to adverse flow interactions, while metal foams achieve only modest tonal gains [12]. Stochastic foams and granular materials disrupt airflow unevenly, boosting pressure drop and undermining aerodynamic efficiency. Likewise, honeycomb liners require large $\lambda/4$ cavities to target low-frequency noise, significantly increasing weight and volume. In sum, traditional materials lack precise topology control and tunability, and few studies have explored multi-parameter optimizations for varying frequencies or operating conditions [13]. In contrast, acoustic metamaterials bring a fundamentally different approach. Their continuous, minimal-surface geometries create programmable pore networks that deliver consistent broadband absorption and multi-order tonal suppression without compromising airflow [14]. By leveraging additive manufacturing, designers can precisely tailor pore shape, size, orientation, and overall porosity to specific noise spectra and aerodynamic loads. Near-zero-mean-curvature surfaces minimize pressure losses, preserving fan efficiency even as they significantly attenuate both low- and mid-frequency noise [15]. While these solutions have been proven with success, the use of TPMS-based porous casings as a solution to reduce noise is not well explored and thus allows for research gaps. In contrast to conventional porous materials, this work pioneers the application of TPMS structures specifically for axial fan tip-leakage noise control: a gap previously unaddressed in literature. The current study bridges this gap by introducing the first application of TPMS casings to control tip-leakage noise in axial fans. TPMSs are mathematically described by smooth, non-intersecting, 3D surfaces that have zero mean curvature at each three dimensional point. These structures repeated along three directions form mutually entangled domains with distinctive acoustic and mechanical properties [16]. TPMS structures attenuate aeroacoustic noise at its origin by breaking up tip-leakage vortices through their continuous, interconnected cell networks. Their complex topology and multifunctional nature deliver outstanding energy dissipation, vibration damping, and overall noise suppression compared with conventional bulk materials and fibrous absorbers [17]. TPMS structures, in contrast to traditional foams and fibers, demonstrate advanced acoustic performance and mechanical strength, resulting in superior durability and efficiency [18, 19]. Most notably, the Diamond-type TPMS demonstrates excellent sound absorption in the upper midrange frequency range (2000–6000 Hz), which is crucial to human hearing acuity [20]. This increases tortuosity and leads to their high absorption coefficients due to increased airflow pathways and improved viscous dissipation of the sound waves. Moreover, TPMS structures can achieve low band gaps at wide frequency ranges (>6000 Hz), outperforming conventional absorbers that only target the narrowband or low frequency [21, 22]. Because they absorb energy in modes other than just transmission and reflection, they are particularly useful for vibration and noise control. The advancements in additive manufacturing were brought that allow for the fabrication of complex designs with precision, providing for the ideal use of materials for the best possible performance while minimizing the volume and overall mass footprints to support

industrial applications. The versatility of TPMS structures allows them to be implemented as device structures in various engineering fields to achieve excellent acoustic and mechanical energy absorption performance [23].

The current study attempts to bridge this gap by exploring the application of TPMS structures as an alternative means of noise mitigation in AFFs. In contrast, research by Bowen et al. [24], that these structures had proven successful in aerospace applications. For the first time, these structures are used in noise reduction of AFFs. We adapt TPMS casings specifically for fan tip-leakage noise control. By leveraging additive manufacturing, we can precisely adjust pore geometry, size, and orientation to meet specific acoustic targets. This geometric tunability enables wide-band absorption, with a focus on low- to mid-frequency ranges that conventional foams and MPPs struggle to address. We place equal emphasis on preserving aerodynamic performance, aiming for noise reduction without any measurable efficiency loss. Our approach directly addresses the multi-parameter optimization gap :conventional porous liners lack the flexibility to tune for varying flow and frequency conditions. Through combined numerical simulations and experimental tests, we examine how different TPMS designs influence airflow patterns and sound radiation mechanisms. Preliminary findings indicate substantial reductions in blade-pass tonal peaks and broadband hiss, achieved with minimal added pressure drop. The versatility of TPMS casings makes them suitable for a range of fan applications. While maintaining structural integrity and light weight. Ultimately, this work lays the foundation for next-generation fan noise control, showcasing TPMS-based porous treatments as a superior alternative to traditional liners and foams.

Both oriented numerical and experimental investigations of the aeroacoustics of TPMS-based porous casings are carried out to emphasize their influence on noise generation as well as flow features in AFFs. The outline of this paper is as follows: Sections 2 (Materials and methods) and 3 (Results and discussion).

2- Materials and Methods

In our numerical study, we conducted aerodynamic and aeroacoustic simulations using the lattice-boltzmann method (LBM) and large eddy simulation. Both methods rely on key governing equations. In this section, we explain these equations along with the simulation materials needed.

2-1- Lattice Boltzmann Method

The Lattice-Boltzmann method adopts a mesoscopic approach, modeling fluid dynamics through particle interactions on a regular lattice. Fluid flow emerges from the collective behavior of these particles, with the Boltzmann equation using a single density function, f, to represent each particle's state [25].

$$\frac{\partial f}{\partial t} + \overrightarrow{v} . \nabla f = \Omega (f) \tag{1}$$

Here, $f(\vec{x},\ \vec{v}, t)$ represents the probability of encountering other particles with continuous microscopic velocity $\vec{c} = \Delta x/\Delta t$, at position *x* and time *t*. The collision operator $\Omega\ (f)$ governs the rate of change in *f* during collisions.

In many kinetic theory applications of fluid dynamics, the collision term $\Omega\ (f)$ is represented by a complex integral. However, the Bhatnagar-Gross-Krook (BGK) approximation simplifies this by replacing the integral with a more manageable expression [25].

$$\Omega\ (f) = \frac{1}{\tau}\left(f_i^{eq} - f_i\right) \tag{2}$$

This operator models collisions by relaxing the distribution function *f* toward the Maxwellian equilibrium state f_i^{eq}. The parameter τ determines the relaxation time, controlling how quickly *f* approaches equilibrium.

To discretize the Boltzmann equation, the continuous velocity space is reduced to a finite set of velocities $\{\vec{e_0}, \vec{e_1}, \ldots, \vec{e_{n-1}}\}$. The distribution function *f(x ⃗, v ⃗, t)* is then represented as a set of functions $f_i(\vec{x}, t)$, each corresponding to transport along its respective velocity vector $\vec{e_i}$. The total probability density function is given by $f = \sum_{i=0}^{n-1} f_i$, which, under proper normalization with a reference density ρ_0, corresponds to the fluid density $\rho(\vec{x}, t)$.

Under the BGK approximation, the Boltzmann equation transforms into a set of discrete lattice Boltzmann equations [25]:

$$\frac{df_i}{dt} + \vec{e_i}\,.\nabla f_i = \frac{1}{\tau}\left(f_i^{eq} - f_i\right) \tag{3}$$

The equation is discretized with a spatial step $\Delta\vec{x}$ and a time step Δt, which are related. The lattice is structured so that particles at node $\vec{x}$ move precisely to the neighboring node $\vec{x} + \vec{e_i}\,\Delta t$ along the velocity vector $\vec{e_i}$ in time Δt.

A splitting approach is typically used, where particles first propagate along lattice bonds to neighboring nodes during Δt, followed by the collision step:

$$\tau:\ f_i^*(\vec{x} + \vec{e_i}\,\Delta t, t + \Delta t) = f_i(\mathbf{x}, t) \tag{4}$$

This step, known as streaming, is followed by a collision step, where arriving particles interact and adjust their velocity directions. This interaction is handled by numerically integrating the right-hand side of equation (2):

$$C:\ f_i(.\,, t + \Delta t) = f_i^*(.\,, t + \Delta t) + \frac{\Delta t}{\tau}\left(f_i^{*,eq}(.\,, t + \Delta t) - f_i^*(.\,, t + \Delta t)\right), \tag{5}$$

LBM schemes are classified based on spatial dimension *d* and the number of distribution functions *b*, denoted as *DdQb*. In two dimensions, a common model uses nine discrete velocity directions, forming the *D2Q9* lattice structure. The unit velocity vectors for this stencil are [25]:

$$\overrightarrow{e_i} = \begin{Bmatrix} 0, \\ (\pm 1, 0)c, (0, \pm 1)c \\ (\pm 1, \pm 1)c \end{Bmatrix} \begin{matrix} i = 0 \\ i = 1, 2, 3, 6 \\ i = 4, 5, 7, 8 \end{matrix} \quad (6)$$

the discretized equilibrium distribution function for the *D2Q9* model typically takes the following form [25]:

$$f_i^{eq} = \rho \omega_i \left(1 + \frac{3}{c_s}(e_{ia} u_a) + \frac{9}{2c_s^2}(e_{ia} u_a)^2 - \frac{3}{2c_s^2}(u_a)^2 \right) \quad (7)$$

In the expression, e_{ia} and u_a represent the components of the unit velocity vector $\overrightarrow{e_i}$ and the macroscopic flow velocity vector $\vec{u}$ in direction a, respectively. The flow velocity $\vec{u}$ is calculated from the first moment of the distribution functions, given by [25]:

$$\rho(\vec{x}, t) u_a(\vec{x}, t) = \sum_i \overrightarrow{e_{ia}} f_i(\vec{x}, t) \quad (8)$$

The coefficients in equation (7) are derived from isotropy arguments and are given by:

$$\omega_i = \begin{Bmatrix} 4/9, \\ 1/9 \\ 1/36 \end{Bmatrix} \begin{matrix} i = 0 \\ i = 1, 2, 3, 6 \\ i = 4, 5, 7, 8 \end{matrix} \quad (9)$$

The speed of sound is $c_s = c/\sqrt{3}$, and the pressure is obtained from the equation of state: $p = c_s^2 \rho$ This demonstrates that the LBM is derived under isothermal conditions, where it only captures pressure fluctuations around a reference pressure p_0, which can be arbitrarily chosen. Such methods are referred to as *weakly compressible*. Additionally, it can be shown that the kinematic viscosity v and collision time τ are related by the following equation [25]:

$$\tau^{-1} = \frac{c_s^2}{v + \Delta t \, c_s^2/2} \quad (10)$$

While the basic model is suitable for simulating laminar flows, a turbulence model is required for high Reynolds number cases. In the context of LBM, the most common approach is to use large eddy simulation (LES) to model turbulence.

2-2- Turbulence Modeling

Turbulent flows are characterized by eddies that span a wide range of length and time scales. To model this turbulence, the Large Eddy Simulation (LES) approach is used. In LES, large eddies are directly resolved, while small eddies are modeled. To account for subgrid turbulence, additional viscosities, known as turbulent eddy-viscosity (v_t), are introduced. The specific LES model employed is the Wall-Adapting Local Eddy (WALE) model, which simulates local eddy-viscosity and near-wall behavior. This model uses a filter scale $\Delta f = C_w \Delta x$, where Δx, is the grid

size and C_w is a constant coefficient (set of 0.325). The strain rate tensor $S_{\alpha\beta}$ for the resolved scales, and the local strain rate tensor $g_{\alpha\beta}$, are computed using the Lattice-Boltzmann method as a second-order momentum [26].

$$v_t = \Delta_f^2 \frac{\left(G_{\alpha\beta}^d G_{\alpha\beta}^d\right)^{\frac{3}{2}}}{\left(S_{\alpha\beta}S_{\alpha\beta}\right)^{\frac{5}{2}} + \left(G_{\alpha\beta}^d G_{\alpha\beta}^d\right)^{\frac{5}{4}}} \tag{11}$$

$$S_{\alpha\beta} = \frac{g_{\alpha\beta} + g_{\beta\alpha}}{2} \tag{12}$$

$$G_{\alpha\beta}^d = \frac{1}{2}\left(g_{\alpha\beta}^2 + g_{\beta\alpha}^2\right) - \frac{1}{3}\delta_{\alpha\beta}g_{\gamma\gamma}^2 \tag{13}$$

$$g_{\alpha\beta} = \frac{\partial u_\alpha}{\partial x_\beta} \tag{14}$$

2-3- Aeroacoustics Analysis

The LBM is inherently unsteady and compressible, allowing Direct Noise Computation (DNC). The numerical speed of sound is matched to the thermodynamic speed of sound through the time step selection [27]:

$$c_{num} = \frac{dx}{\sqrt{3}dt}, \qquad c_s = \sqrt{\frac{\gamma RT}{M}}, \qquad c_{num} = c_s, \qquad dt = \frac{dx}{\sqrt{3}c_s} \tag{15}$$

Here, *dx* denotes the lattice spacing and *dt* the time step. The factor $1/\sqrt{3}$ stems from the lattice isotropy requirements and depends both on the chosen lattice scheme and on the collision operator. In these expressions, γ is the adiabatic index, *M* the molecular weight, *R* the universal gas constant, and *T* the operating temperature.

The lattice-Boltzmann method also has the great advantage of including easily the bulk viscosity, also called volume viscosity, which can be recovered by redefining the equilibrium distribution function. Bulk viscosity ($\mu_V = \mu' + \frac{2}{3}\mu$) is included to account for compressibility effects, appearing in the Navier-Stokes equation [27]:

$$\rho\left(\frac{\partial \mathbf{v}}{\partial t} + \mathbf{v}\cdot\nabla\mathbf{v}\right) = -\nabla p + \mu\nabla^2\mathbf{v} + \mathbf{f} + (\frac{1}{3}\mu + \mu_V)\nabla(\nabla\cdot\mathbf{v}) \tag{16}$$

This inclusion is vital for capturing compressibility-related acoustic phenomena. Also, to ensure accurate acoustic wave propagation, XFlow uses Local One-Dimensional Inviscid (LODI) equations for non-reflective boundaries. At each non-reflecting boundary patch, the solution vector *U* (containing density, momentum components, and energy) is advanced according to a one-dimensional inviscid wave equation in the normal direction *x* [27]:

$$\frac{\partial U}{\partial t} + \Gamma_x \frac{\partial U}{\partial x} = 0 \tag{17}$$

Here, Γ_x is the flux Jacobian in the boundary-normal direction and amplitudes [27]:

$$L = \big((u_x - c_s)(\partial p/\partial x - \rho c_s\, \partial u_x/\partial x), u_x\, \partial u_y/\partial x, u_x(c_s^2\, \partial \rho/\partial x - \partial p/\partial x), (u_x + c_s)(\partial p/\partial x + \rho c_s\, \partial u_x/\partial x)\big) \tag{18}$$

This approach minimizes reflections at boundaries, enhancing the accuracy of far-field acoustic predictions. XFlow computes pressure wave propagation directly, capturing pressure fluctuations over time. This is achieved by simulating the flow field and extracting pressure data at points of interest, which is then used for acoustic analysis. Also, XFlow offers a suite of post-processing features (FFT and SPL) for acoustic analysis, enabling detailed spectral processing.

2-4-Modeling Workflow and Boundary Conditions

In this study, an aerodynamic-acoustic simulation was conducted on a 7-blade axial flow fan designed for computer cooling, with a 120 mm diameter, using XFlow software. The geometry and parameters of the fan are shown in **Figure 1** and **Table 1**. To model the fluid flow, the WALE model was implemented due to its effectiveness in handling both near-wall and turbulent flow conditions. For the acoustic analysis, the DNC method was applied within XFlow to capture noise propagation accurately. The computational domain was defined as a rectangular box with dimensions 7.2 m (length) × 2.4 m (width) × 2.4 m (height). The fan was positioned at the center of the x-y plane, 2.4 m away from the left wall. To simulate fan rotation, the Arbitrary Reference Frame (ARF) method was used instead of actual moving geometries. This approach significantly reduces computational time by eliminating the need for geometry displacement, while still allowing for accurate visualization of output data relative to the chosen reference frame. Our choice of this method over Immersed Boundary Method (IBM) approach is supported by validated axial-fan benchmarks, where rotating-frame approaches consistently reproduce broadband spectra and are more widely applied [28, 29]. In contrast, applying IBM to a highly porous, stationary casing would demand extremely sharp interfaces and dense grid refinement to avoid numerical permeability and damping, leading to high computational cost despite IBM's strength in capturing unsteady blade dynamics [30]. The rotating frame was set to operate at a speed of 1200 rpm. For numerical stability, the Courant number was set to 1, and the non-equilibrium enhanced wall function was employed for wall treatment. Air was selected as the working fluid, with boundary conditions carefully defined to ensure accurate simulation results. Both the inlet and outlet boundaries were set as pressure outlets with a 0 pascal value (ambient), while the side walls of the computational domain were treated as far-field boundaries. Additionally, the fan and casing surfaces were modeled as walls with a no-slip condition, ensuring realistic airflow interactions. **Figure 2** provides a detailed illustration of the computational domain, boundary conditions, fan geometry, and positioning used in the simulation.

Table 1. The detailed parameters used in AFF design.

Casing axial length L (mm)	28
Hub radius h (mm)	23
Rotational speed (rpm)	1200
Casing outer radius r_o (mm)	60
Casing inner radius r_i (mm)	57
Hub axial length w (mm)	22
Tip Clearance tc (mm)	2

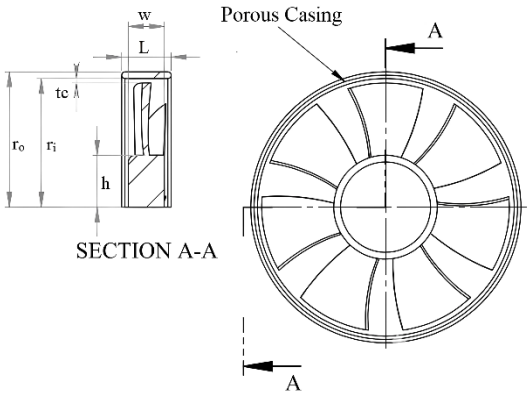

Figure 1. The AFF's geometric requirements.

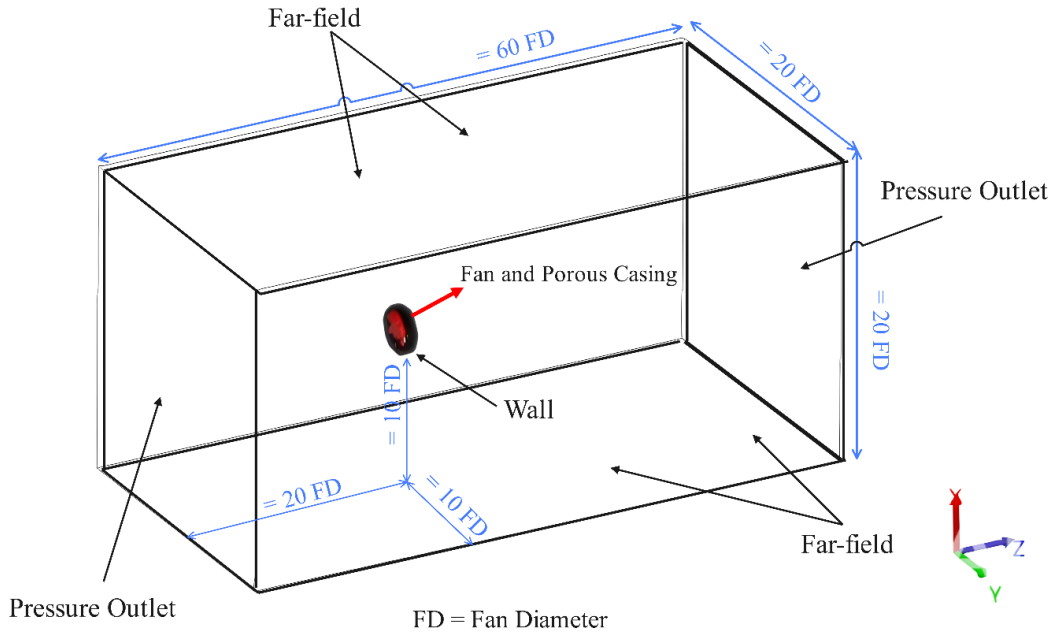

Figure 2. Computational domain and boundary conditions for simulation.

2-5- Automatic Lattice Generation

One of XFlow's major strengths is its lattice-Boltzmann method (LBM), which completely removes the need for manual mesh generation. Instead, XFlow builds an orthogonal Cartesian lattice that automatically refines by factors of two (resolution= $x/2^n$ for integer n) in critical regions (such as around the fan and casing) while keeping the far field coarser. This adaptive lattice is stored efficiently in an octree structure, greatly reducing setup time and the risk of meshing errors compared to traditional Navier–Stokes CFD workflows [31].

Figure 3 illustrates this multi-level Cartesian discretization for a generic rectangular domain. By combining fine and coarse lattice blocks only where needed, XFlow achieves high local accuracy without wasting computational resources on unnecessary refinement. For this simulation, the resolved scale value for the lattice is set to 0.1 m, while the target resolved scale value for the fan

and casing is set to 0.0001 m. additionally, adaptive refinement is applied to dynamically refine moving objects, ensuring accurate and efficient computations.

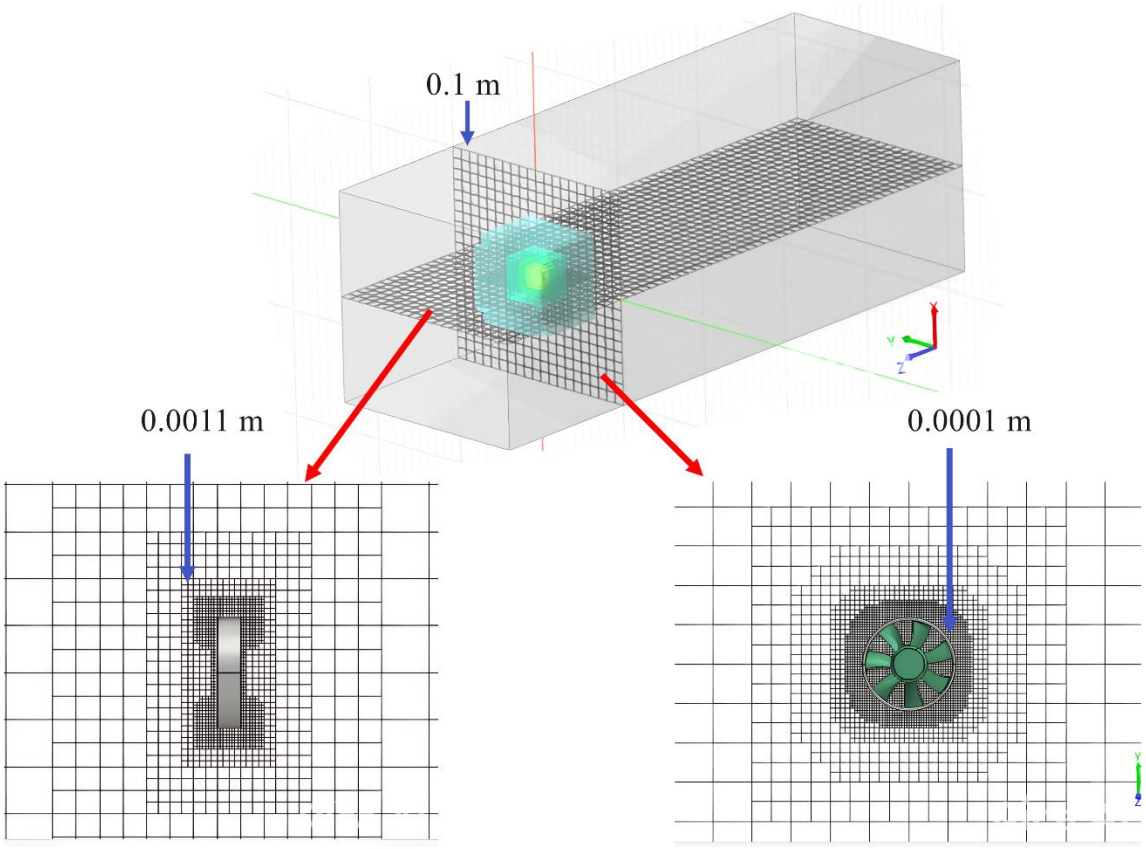

Figure 3. Discrete schematic diagram of domain space and planes.

2-6- The TPMS Casing Treatment and Experimental Setup

The most well-known and widely used TPMS structures include Diamond and Gyroid. To generate the porous casing, a Matlab code was developed, allowing for the creation of different casings based on porosity percentage and TPMS type. These structures were then fabricated using 3D printing and tested acoustically in an anechoic chamber with a cutoff frequency of 100 Hz. After 3D printing, all TPMS casings were immersed in an ethyl acetate bath to eliminate surface irregularities, yielding a uniformly smooth finish. **Figure 4** presents the produced casing alongside the fan geometry with the porous casing. The acoustic measurements were conducted using a PreSonus® PRM1 microphone, which has a frequency range of 20 Hz to 20 kHz and a sensitivity of 14 mV/Pa, with each recording lasting 20 seconds (as shown in **Figure 5**). The collected data was then processed in Matlab, where it was converted into a sound pressure level (SPL in dB) curve. In previous research [20], comprehensive experimental tests were conducted, and their results served as a benchmark to validate the numerical simulation outcomes.

(a) Photograph of the fan with casing

(b) Printed model

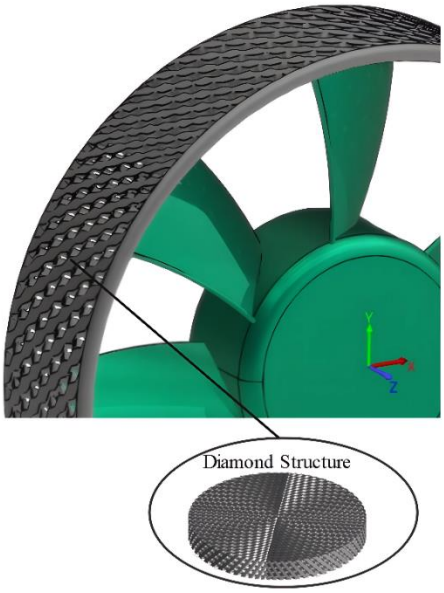

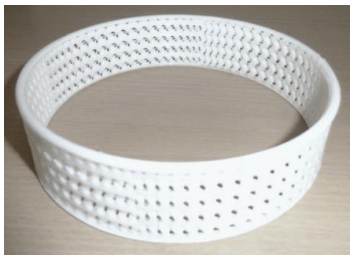

(c) Designed model

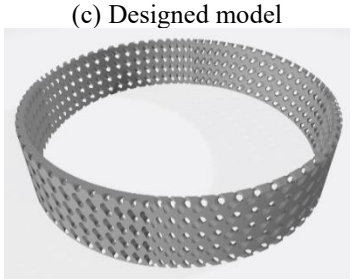

Figure 4. Visualization of a fan featuring a diamond-patterned porous casing.

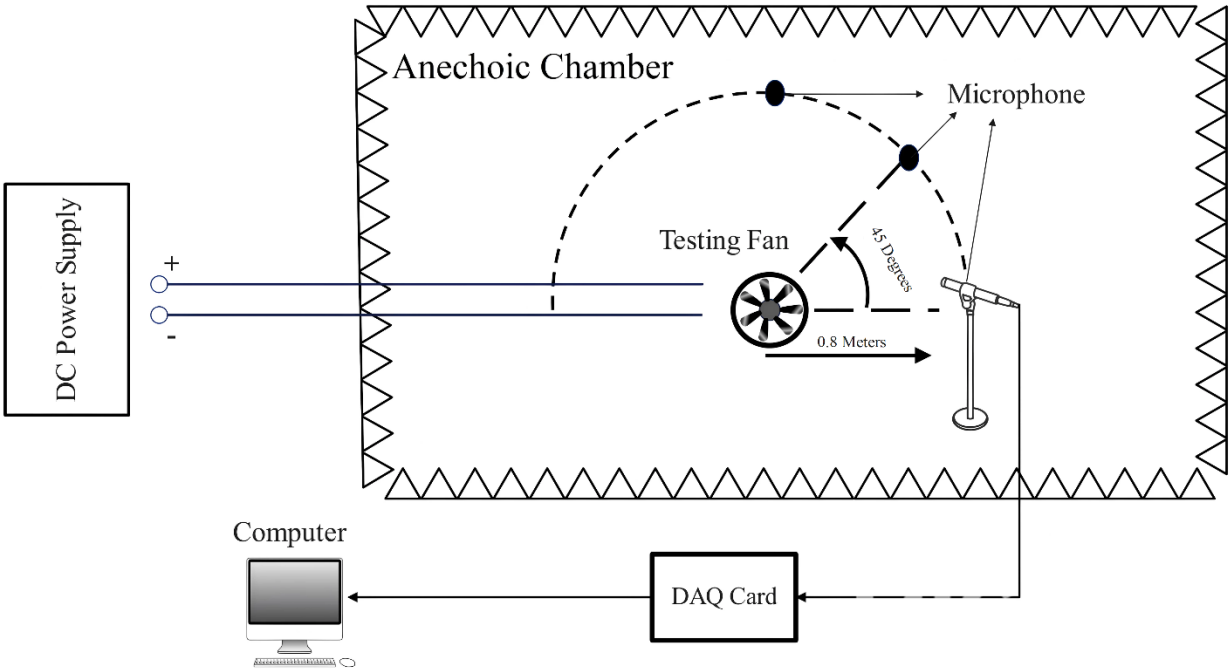

Figure 5. Schematic representation of experimental setup and microphone array.

2-7- Validation

To validate the aeroacoustic simulation results, SPL and OASPL curves for both the solid casing (left) and the porous casing (right) are compared with the experimental acoustic test results [20] shown in **Figure 6**. Both sets of curves display the experimental data (green) alongside the numerical results (black). In both cases, the numerical results slightly overestimate SPL and OASPL compared to the experimental measurements. Although both the experimental tests and

simulations were conducted with high precision, some discrepancies are to be expected, particularly at higher frequencies, where these differences become more pronounced. The simulations don't show clear blade-passing frequency (BPF) or harmonic tones because the quasi-steady ARF method smooths out the rapid pressure changes caused by each blade pass. By averaging the flow over time, ARF filters out those unsteady fluctuations that create the distinct tonal peaks. Moreover, the discrepancy observed in the OASPL curve remains below 8%, potentially attributable to repeatability error margins. Several factors could contribute to these differences, including approximations or simplifications within the numerical model that may not fully account for all real-world variables, such as precise material properties, boundary conditions, or the complex interactions between the fan and the casing. Furthermore, the experimental results could be influenced by external factors, such as thermodynamic conditions or microphone placement, which may cause variations in the SPL compared to the ideal conditions assumed in the simulation. Despite these minor differences between the experimental and numerical results, the overall trends are consistent, and the simulation provides a reliable representation of the fan's acoustic behavior. LBM with LES turbulence modeling accurately estimates of the acoustic performance of the flow around the axial flow fan.

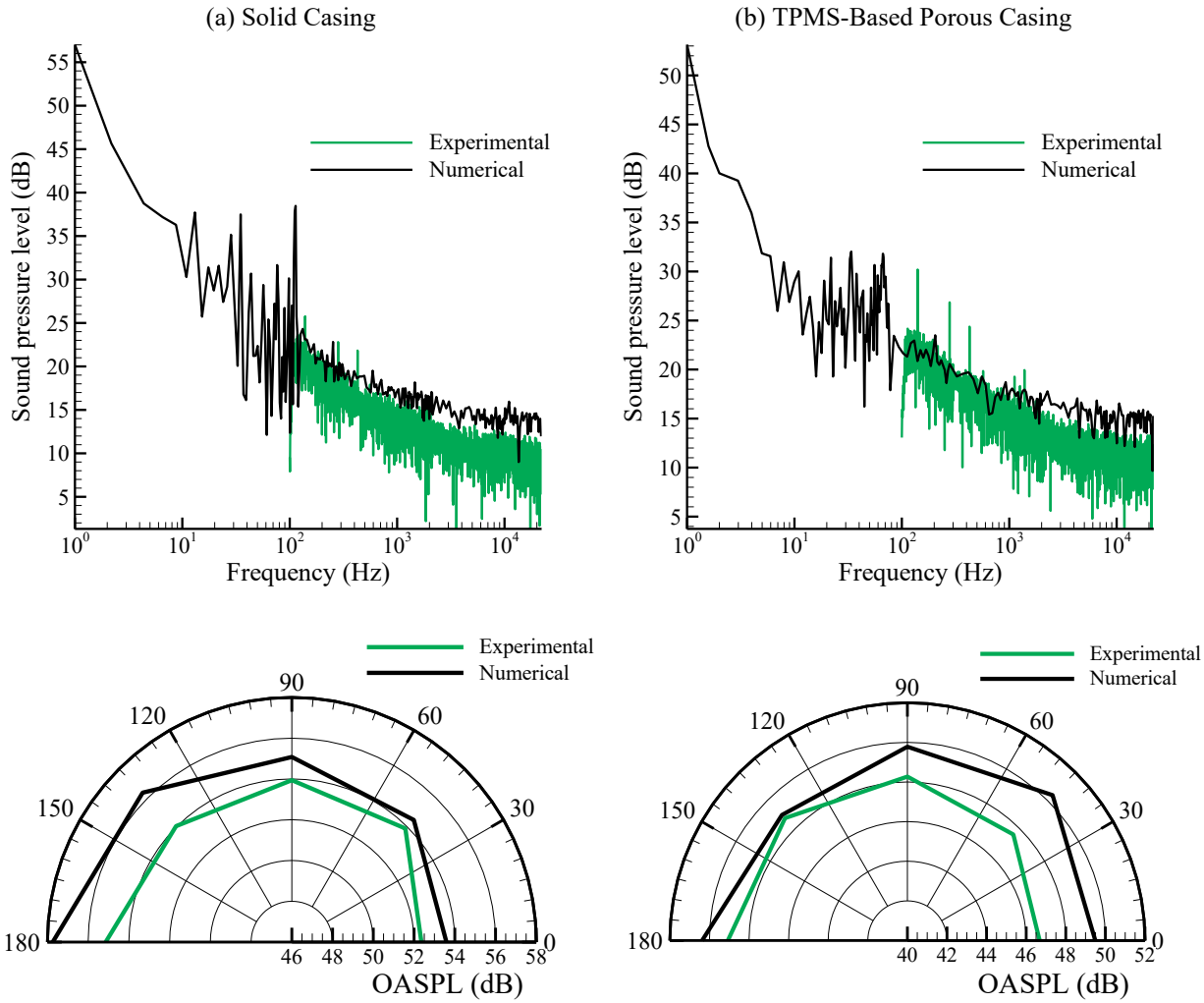

Figure 6. Numerical simulation validation: measurements were taken at 0.8 m distance and a 45° angle to the horizontal axis, at a rotational speed of 1200 rpm.

3- Simulation Results

3-1- Noise Reduction with TPMS-Based Porous Casings

Figure 7 illustrates the Insertion Loss (in dB) as a function of frequency (in Hz) for three different TPMS structures: Diamond 50% - Its porosity percentage is 50%- (black), Gyroid 50% (orange), and Diamond 35% (dashed line). In this context, insertion loss refers to the reduction in noise due to the change in the casing and the placement of a porous casing instead of a solid casing in the path of sound waves ($IL(f) = SPL_{solid}(f) - SPL_{porous}(f)$). The aim is to identify which structure exhibits the highest insertion loss, thereby demonstrating better sound absorption or reflection performance. The data reveals that the Diamond 50% structure achieves the highest insertion loss across the frequency range, particularly at higher frequencies, indicating superior sound attenuation. In comparison, the Gyroid 50% structure offers a lower insertion loss than the Diamond, showing effective sound absorption, though its performance is less consistent across the frequency spectrum. Finally, the Diamond 35% structure displays the lowest insertion loss overall, suggesting that a reduced volume fraction diminishes the material's ability to attenuate sound. These findings highlight that the volume fraction of a material significantly influences its sound-blocking or attenuation properties. The Diamond structure is particularly effective due to its interconnected cells with sharp angles and varying cross-sectional areas, which scatter sound waves and enhance sound energy dissipation through viscous damping. Additionally, its high surface area-to-volume ratio and complex pore pathways improve sound absorption. On the other hand, the Gyroid structure, with its smooth, curvilinear surfaces and moderate surface area, is less effective in scattering sound compared to the Diamond. Nevertheless, it still offers considerable sound absorption capabilities.

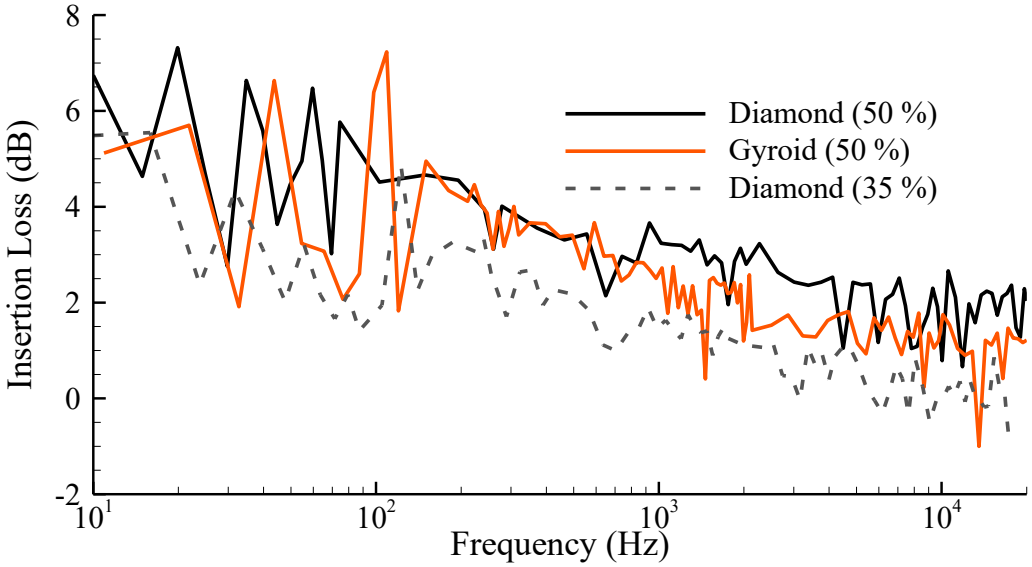

Figure 7. Insertion Loss curve for three different TPMS structures: Diamond 50%, Gyroid 50%, and Diamond 35%.

Figure 8 presents the profiles of radial fluctuation velocity and turbulence intensity (TI) both in front of the fan and at a vertical distance from the casing for both the solid and diamond casing configurations. The analysis of radial fluctuation velocity aids in identifying the primary sources

of noise. Additionally, The TI profile plays a critical role in shaping the acoustic characteristics of the low-speed jet, and noise arises primarily from blade interactions and pressure fluctuations. Higher TI is often associated with increased noise levels due to the chaotic flow behavior, which results in more significant sound generation. In Figure 9a, the radial fluctuation velocity for the solid casing increases and reaches its highest point around 20 mm from the fan, likely because sound waves are stronger in that direction and location. After that, the velocity drops as the flow becomes more stable and gets absorbed due to viscosity. With the porous casing, however, the peak happens later and the disturbance is weaker and fades out more quickly (around 40 mm). This shows that the porous casing reduces the strength of the velocity fluctuations compared to the solid one. Because of this, it's likely that the same calming effect happens in other directions too. Figure 9b supports this idea by showing that the overall TI (which includes all fluctuation directions) is lower when using the porous casing. In other words, the presence of the casing induces vortices at both the leading and trailing edges of the fan. Furthermore, the casing clearance and the rotation of the fan contribute to the leakage flow and the formation of tip leakage vortices. These vortices combine behind the fan, raising turbulence intensity, which can amplify noise emissions. As TI directly influences the acoustic output of the fan, higher turbulence levels generally lead to greater noise generation potential. Therefore, strategies that aim to reduce velocity disturbances and control turbulence offer promising approaches to noise reduction. This study demonstrates that incorporating a casing structure to manage turbulence can significantly enhance flow stability, leading to smoother and quieter fan operation. This confirms that the porous material helps reduce airflow disturbances, making the fan operate more smoothly.

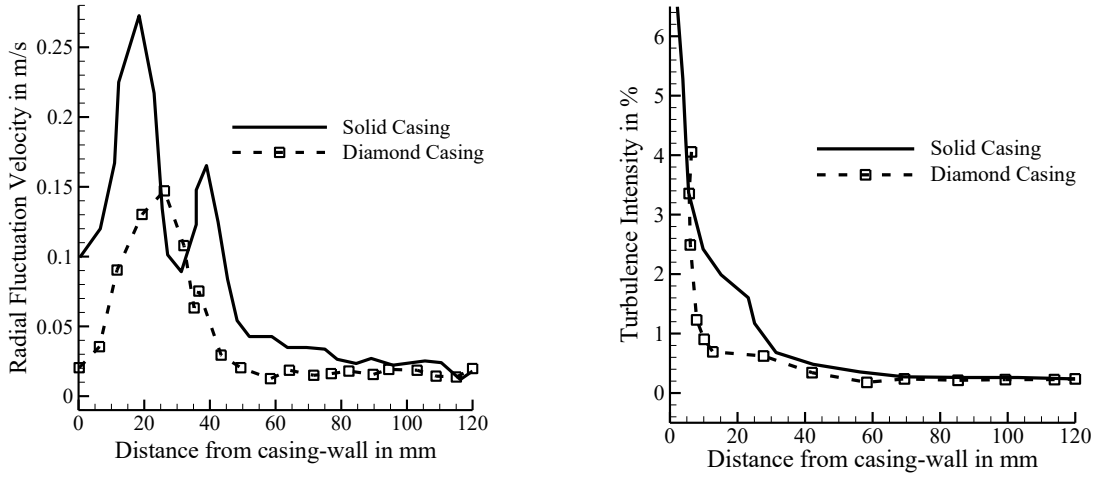

(a) (b)

Figure 8. On the left-hand side, (a) the radial fluctuation velocity profile is presented, while the right-hand side illustrates (b) the turbulence intensity profile measured from the point (0, 60 mm, 16 mm) to the point (0, 180 mm, 16 mm).

In the **Figure 9a** with the solid casing, the fan face displays elevated acoustic pressure fluctuations precisely at the region where tip vortices and wake shedding detach from the blade edges, overlap, and reinforce one another. This bright-red zone lies just ahead of the blade tips and in front of the hub, where the wake from the preceding blade re-impacts the next, generating intense turbulence. The fan's rotation direction skews the fluctuation distribution, and noise propagation paths emanate from the moving blade edges toward the inlet and inner casing wall. By contrast, in the

Figure 9b with the porous casing, although the peak positive acoustic pressure still reaches about +1.0 Pa, the red zone is markedly contracted and concentrated very close to the hub. The porous structure dissipates acoustic energy through viscous losses within its fine-cell walls and rapidly disrupts coherent vortices, thereby reducing the high-acoustic source regions and effectively attenuating the noise propagation paths.

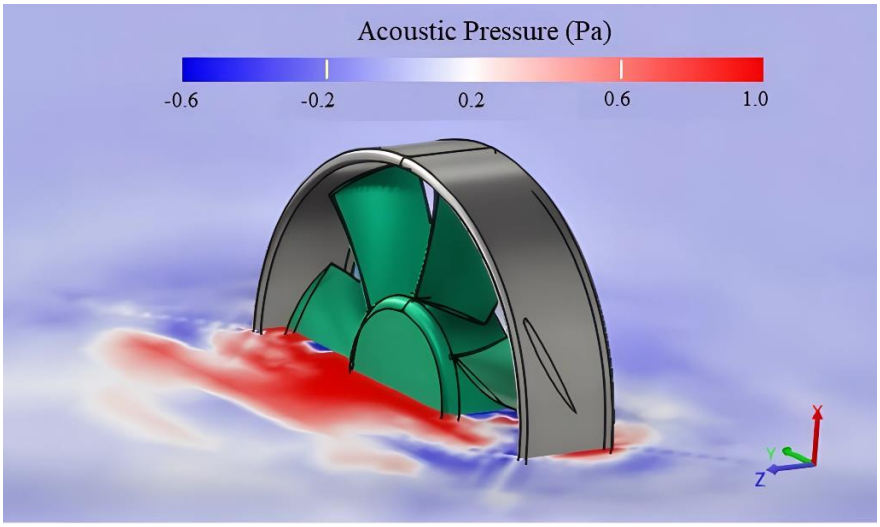

(a) Solid Casing

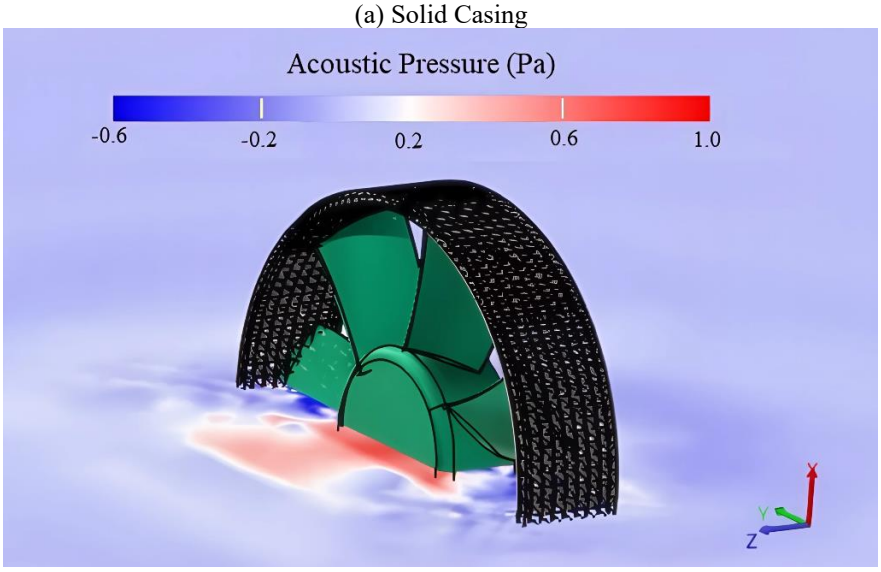

(b) Diamond Porous Casing (50%)

Figure 9. Display the contour of acoustic pressure fluctuations for both (a) solid and (b) diamond casings.

Figure 10 presents the contours of acoustic power (*P*) levels in dB for both the solid and diamond casings at a frequency of 140 Hz, which is near the first blade passing frequency. The figure reveals regions on the inner surface of the casing that contribute significantly to the overall noise generated by the fan and casing. Notably, these regions either shrink in size or exhibit reduced source strength when the diamond-patterned porous casing is used. This reduction in acoustic power levels highlights the enhanced effectiveness of the noise control measures implemented, demonstrating the superior noise attenuation properties of the diamond-patterned casing.

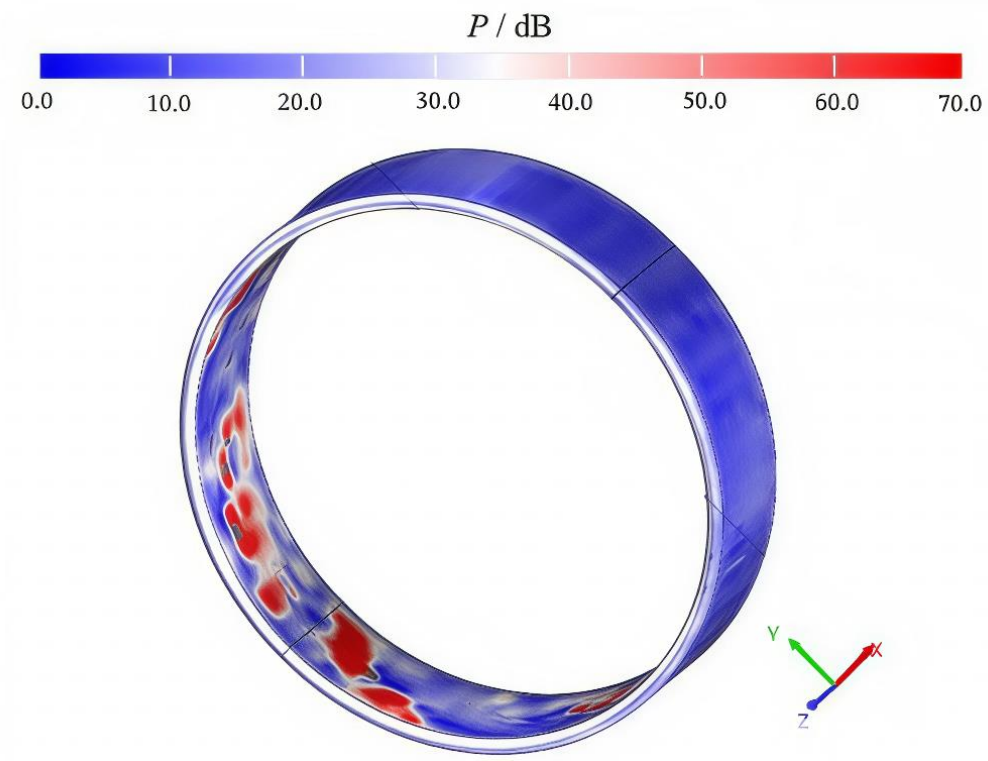

(a) Solid Casing

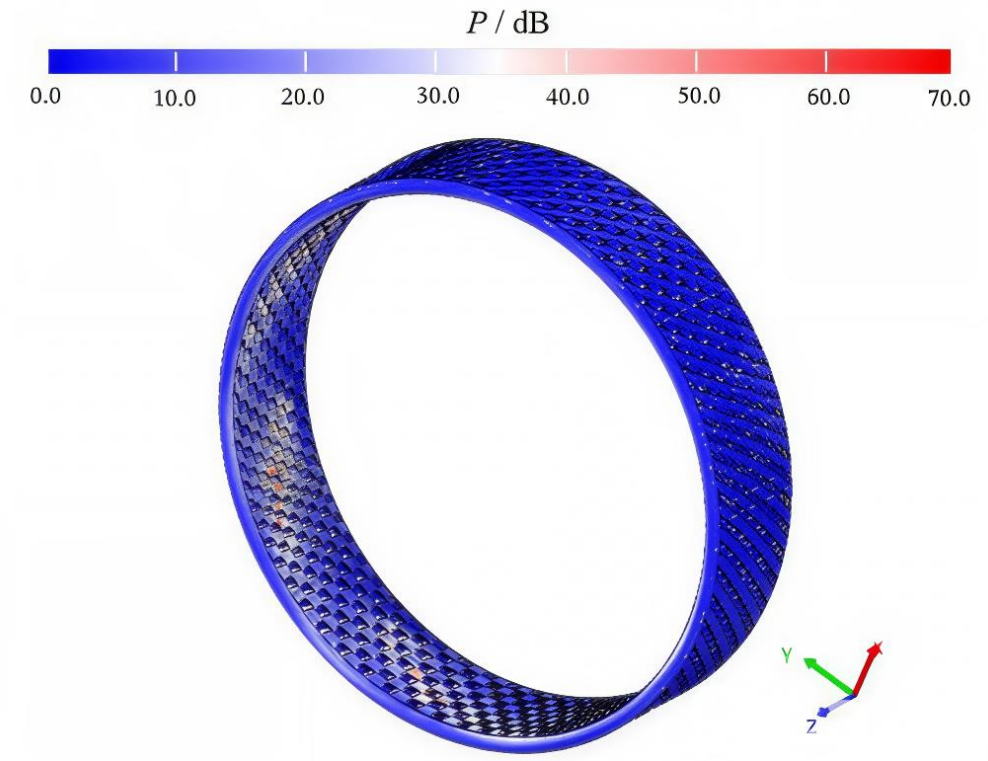

(b) Diamond Porous Casing (50%)

Figure 10. Display the contour of acoustic power levels (*P*) for both solid and diamond casings at BPF1.

3-2- Concept of the Fan Noise Reduction Mechanisms

In the previous section, the aeroacoustic behavior of axial flow fans with TPMS-based porous casings was explored, demonstrating the effectiveness of TPMS structures in reducing noise. In this section, we delve into the underlying factors contributing to this noise reduction. To better understand these mechanisms, we present several aerodynamic characteristics of the flow.

Figure 11 compares the streamlines around the fan and near the casing for three configurations: Solid Casing (SC), Diamond Porous Casing 35% (PC1), and Diamond Porous Casing 50% (PC2). The presence of the porous casing has a significant impact on the streamlines, the flow absolute velocity, and the formation and behavior of tip leakage vortices (TLVs) in small axial flow fans. The porous casing effectively suppresses TLVs, as illustrated in the streamlined structure, where the flow appears more organized and less turbulent compared to a conventional casing. The change in color from dark red to light blue in the flow field shows a drop in absolute velocity. Additionally, as seen in **Figure 13** the flow direction has shifted away from the direction of rotation. This change is expected to weaken the tip vortices, which can help improve the fan's efficiency. By measuring the total pressure rise at a constant flow rate of 65 CFM, the porous casing increased ΔP from 45.6 Pa to 46.1 Pa, yielding a 1.2 % boost in the efficiency of the fan. The simplified flow pattern highlights that the mass flow velocity and average axial velocity decrease when using the porous casing.

Figure 12 presents the vorticity contours for the SC, PC1, and PC2 configurations under identical conditions (same rpm). A comparison of the three contours reveals that the use of porous casing leads to a reduction in the momentum of the tip leakage flow (TLF) when interacting with the main flow. The porous casing effectively diminishes the TLV strength (indicated by black circles). This reduction is primarily attributed to the suppression of the pressure difference between the pressure and suction sides of the blade, which in turn reduces the vortex formation at the fan tip. The flow structure analysis shows that the flow becomes more organized with the introduction of the porous casing, resulting in a decrease in vortex intensity around the tip region. Additionally, in the PC1 and PC2 contours, the strength and size of the vortices shed from the blade are reduced. In particular, in the PC2 configuration, where the volume fraction is higher, the vortex has partially disappeared (highlighted by red arrowheads). The presence of porous casings helps reduce flow instabilities and mitigates noise sources near the fan. This attenuation is advantageous as it minimizes fluctuations that could otherwise lead to increased noise levels and performance instability.

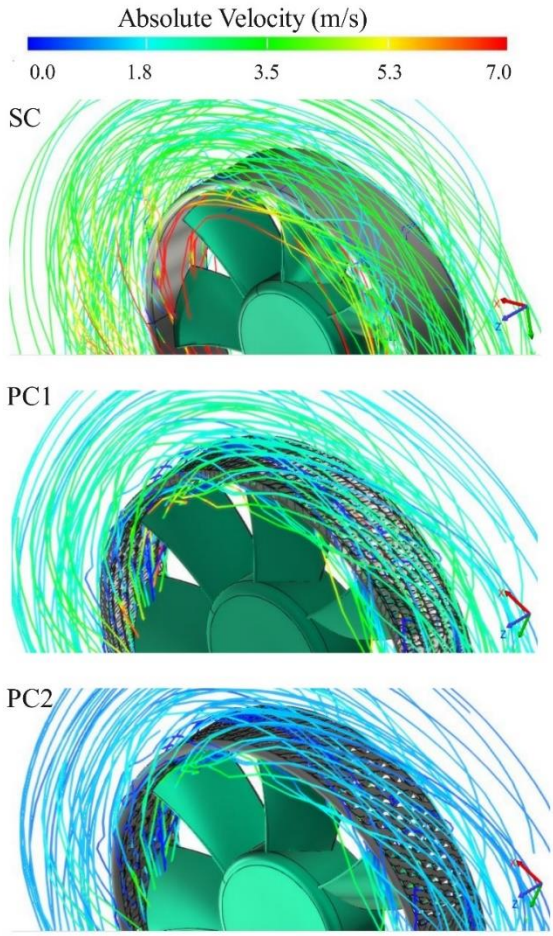

Figure 11. Comparison of the streamlines around the fan and near the casing for three configurations: Solid Casing (SC), Diamond Porous Casing 35% (PC1), and Diamond Porous Casing 50% (PC2).

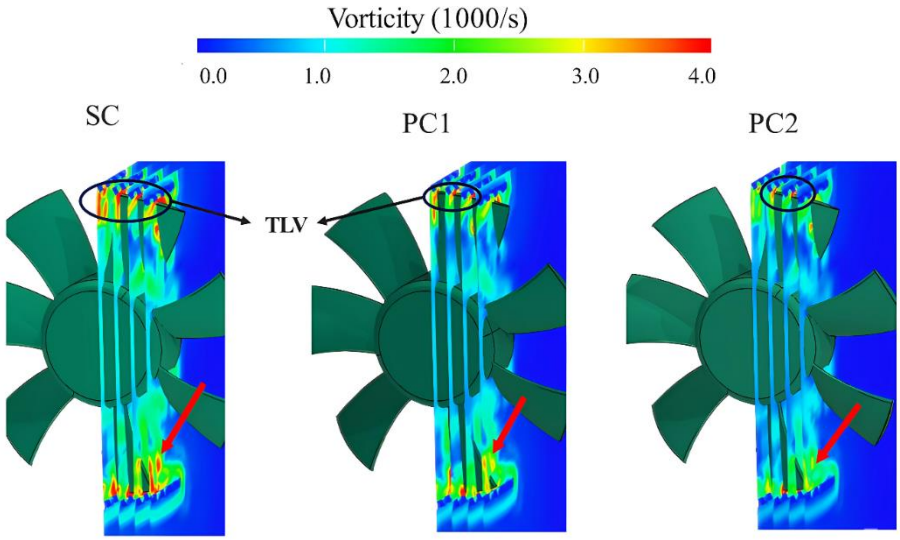

Figure 12. Comparison of the vorticity contours around the fan for three configurations: Solid Casing (SC), Diamond Porous Casing 35% (PC1), and Diamond Porous Casing 50% (PC2).

Figure 13 presents the velocity vector contour for the SC and PC2 configurations under identical conditions (same rpm). The results from these contours reveal that the porous casings have a notable impact on the velocity vectors near the tips of the fan blades, promoting a more uniform velocity distribution across the blade surface. The introduction of the porous casing alters the dynamics of the tip leakage flow by creating secondary flow paths through the fine holes in the casing. This modification helps achieve a more controlled vortex distribution in the tip region, enhancing flow stability. This improvement in flow stability reduces fluctuations and minimizes turbulence, which, as demonstrated in **Figure 8**, leads to lower noise levels. The porous casing reduces velocity fluctuations and shifts the peak fluctuation velocity further away from the casing wall, thereby decreasing turbulence kinetic energy downstream of the fan and relocating noise sources farther from the casing. The velocity vectors near the fluid-porous interface show a gradual decrease in axial velocity as the flow transitions in the porous region. While the velocity at the boundary does not drop to zero, it stabilizes at a relatively constant value, signaling a substantial alteration in flow characteristics due to the porous casing.

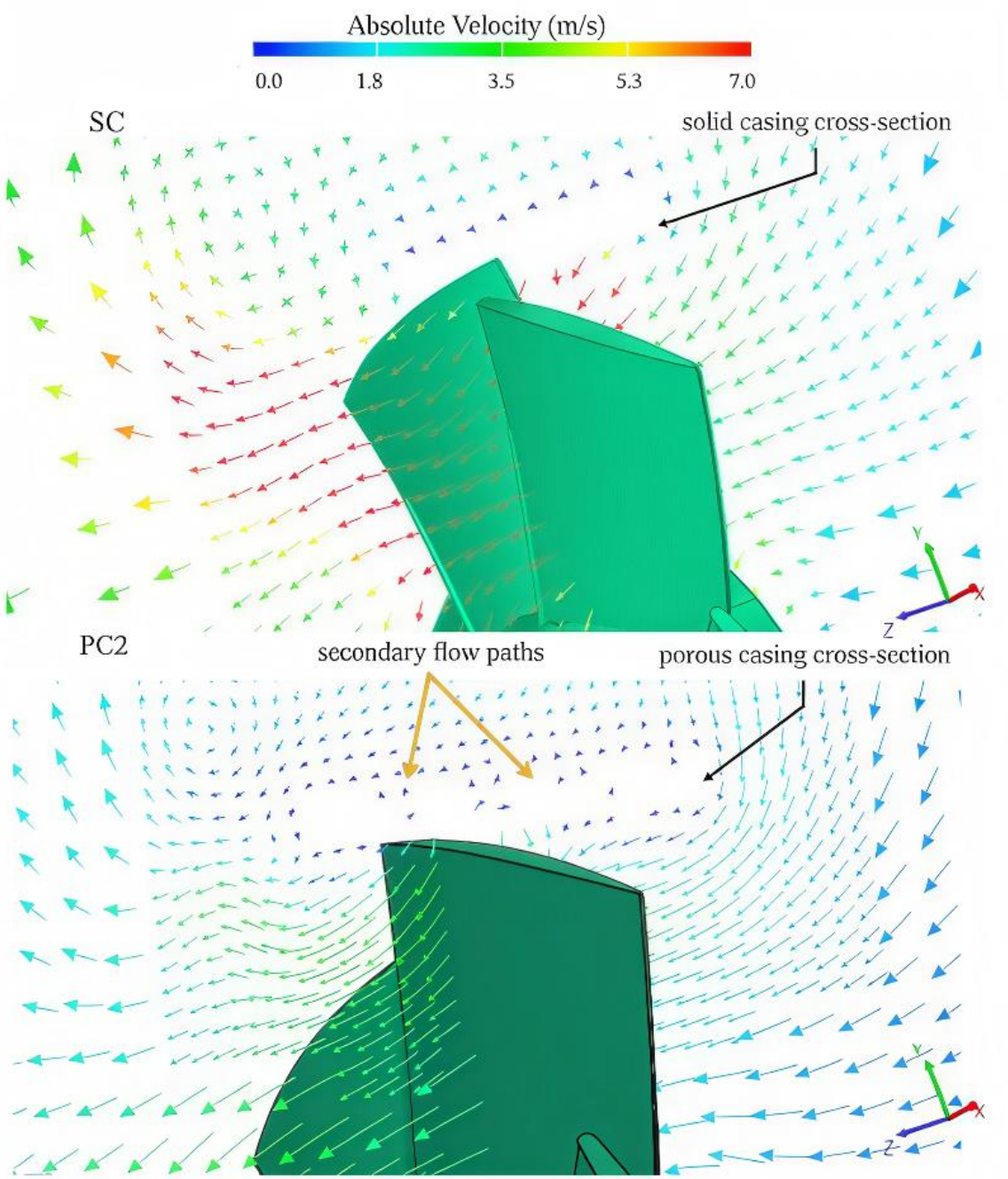

Figure 13. Comparison of the velocity vector contours for both solid and diamond casings on the plane in z direction.

3-3- Selection of the Best Porous Casing Configuration

Noise reduction in TPMS structures is heavily influenced by key geometric parameters, including porosity (p), unit cell size (w), and surface-to-volume ratio. Given their interdependence, it is sufficient to focus on examining either the unit cell size or the surface-to-volume ratio, as both are closely related. As discussed in earlier sections, axial flow fan noise is primarily generated in the lower frequency range, typically between 50 Hz and 250 Hz. In this frequency range, the blade

passing frequency (BPF), its harmonics, and mechanical vibration modes are the dominant sources of noise. Additionally, turbulence interaction and rotor self-noise contribute significantly, although broadband noise at higher frequencies may also be present. Consequently, optimization is crucial to identify the most effective design for minimizing noise based on these factors.

Figure 14 presents the overall noise reduction ($ONR = OASPL_{solid} - OASPL_{porous}$) results for varying porosity percentages and cell sizes. As observed, increasing the porosity percentage generally leads to greater noise reduction. However, excessively high porosity can compromise structural integrity and reduce the effectiveness of acoustic damping if the cell walls become too thin. While porosity is a crucial factor, unit cell size also significantly influences acoustic performance. Modifying the unit cell size alters the surface-to-volume ratio, which in turn affects the overall noise reduction. Furthermore, the relationship between porosity and unit cell size appears to be nonlinear. Therefore, a sensitivity analysis between these two parameters is essential, as optimizing noise reduction requires finding an optimal balance between them.

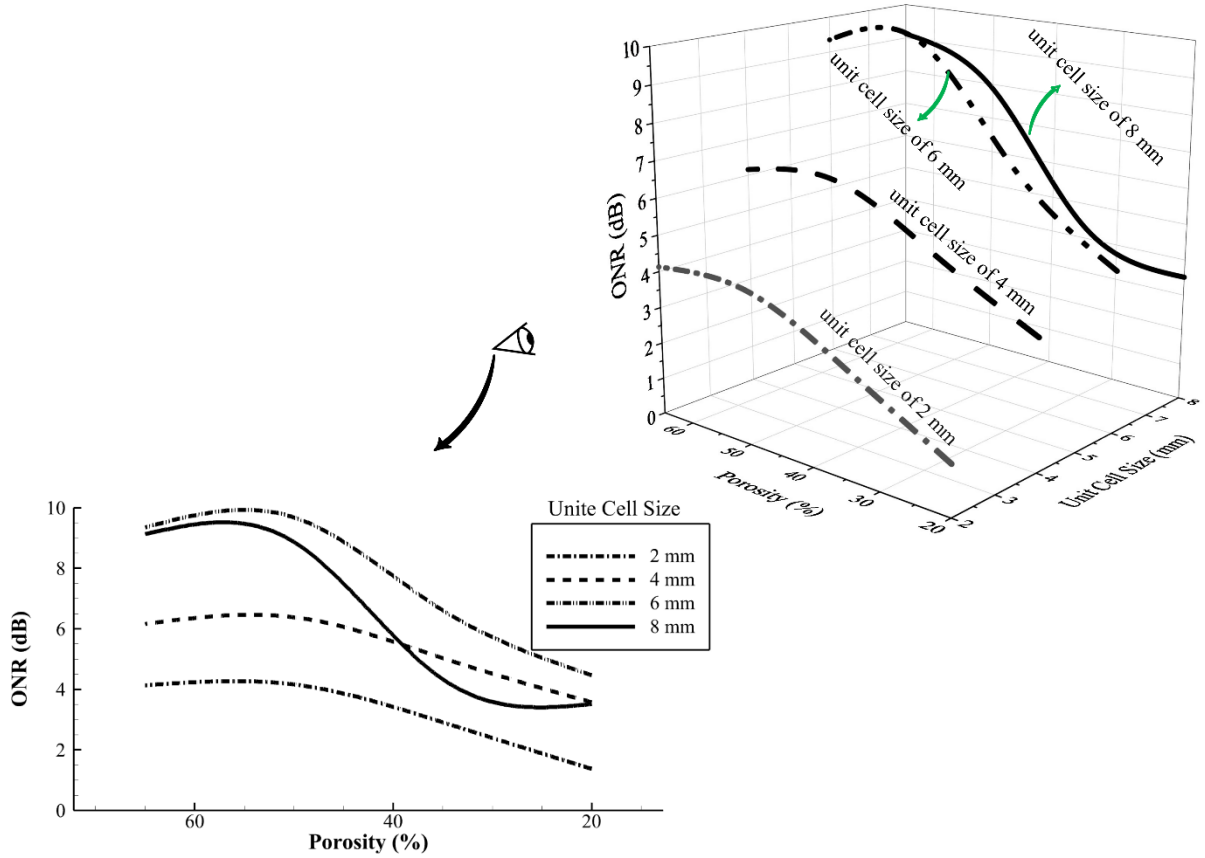

Figure 14. Distribution of overall noise reduction (ONR) based on porosity percentage and unit cell size.

In this section, a MATLAB code has been developed using Response Surface Methodology to analyze and optimize the relationship between unit cell size, porosity, and overall noise reduction. A quadratic model is selected to estimate the ONR relationship, capturing the nonlinear interactions between porosity and unit cell size, to determine the optimal conditions for maximum noise reduction. The resulting relationship for ONR is presented in Equation 15. With an R^2 value

of 0.92, the model shows a strong correlation with the numerical data. The optimization results indicate that the optimal porosity is 55.25%, and the optimal unit cell size is 6.05 mm.

$$ONR = -4.071 + 0.215 \times p + 0.673 \times w + 0.006 \times p \times w - 0.001 \times p^2 - 0.030 \times w^2 \quad (15)$$

Figure 15 presents the optimal results, shown as contour plots. Based on the analysis, a TPMS structure with 55% porosity and a 6mm unit cell size is identified as the optimal configuration for reducing noise in axial flow fans. At approximately ≈ 50% porosity, the structure strikes a balance between effective sound energy dissipation and structural integrity, which is associated with a reduction in turbulence interaction noise. A 6mm cell size is sufficiently large to interact effectively with the long wavelengths of the blade passing frequency and broadband turbulence noise (typically in the 50-250 Hz range), while still maintaining a high surface area for energy dissipation. Smaller cell sizes (2-4mm) would shift the absorption characteristics towards higher frequencies, while larger cell sizes (8mm) may not provide enough internal surface area, reducing their effectiveness in attenuating the low-frequency noise most prevalent in axial flow fans.

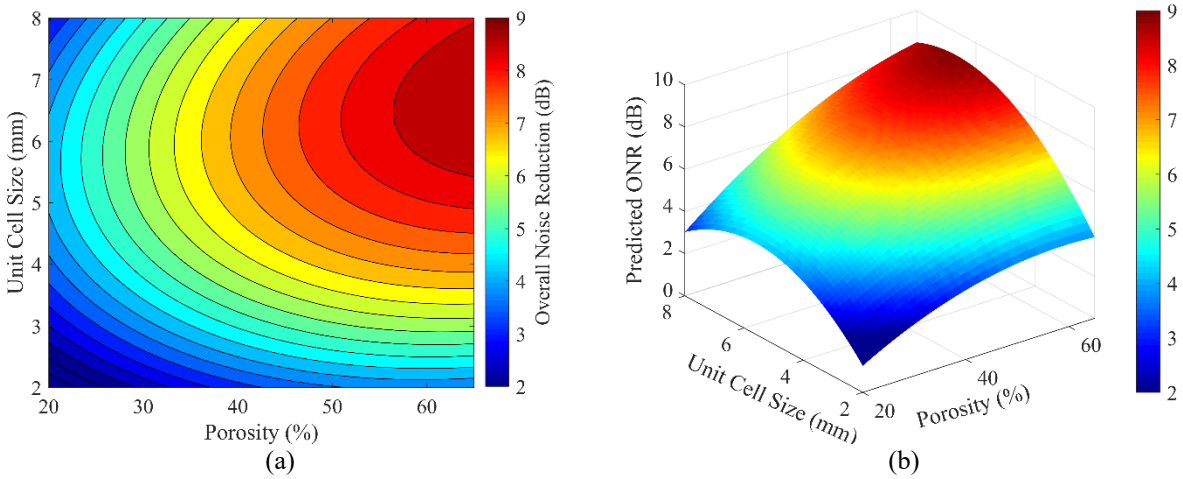

(a) (b)

Figure 15. Visualization of the ONR response, (a) Contour Plot, and (b) 3D Surface.

4- Conclusion

This study explores the aeroacoustic behavior of porous casing treatments for a specific axial flow fan using the Lattice Boltzmann Method and Large Eddy Simulation. Triply Periodic Minimal Surface (TPMS) structures were incorporated into the casing, and their effectiveness in noise reduction was evaluated both experimentally and numerically. The key findings of this investigation are summarized as follows:

1. The effectiveness of TPMS-based casing treatments is highly dependent on geometric parameters and the specific TPMS structure used. Higher porosity percentages and larger unit cell sizes generally enhance noise reduction. Among various TPMS configurations, the diamond structure exhibits superior sound attenuation due to its sharp edges, intricate geometry, and high surface-to-volume ratio. This structure achieves up to a 10 dB reduction in overall noise.

2. Under constant tip clearance and operating conditions, the porous casing significantly weakens and reduces the size of the tip leakage vortex. Additionally, it lowers the absolute velocity, vertical velocity fluctuations, and turbulence intensity near the casing walls. These effects contribute to flow stabilization around the fan blades, ultimately leading to a reduction in radial noise emissions.

3. A comprehensive optimization analysis was conducted to determine the optimal porosity percentage and unit cell size for maximum noise reduction. The results reveal a nonlinear relationship between these parameters. The most effective configuration, offering the highest noise reduction, was found at 55% porosity and a 6mm unit cell size. This optimized design effectively mitigates both blade passing frequency noise and turbulence-induced noise, achieving a well-balanced noise reduction strategy.

Data Availability

The data used to support the findings of this study are available from the corresponding author upon request.

Conflicts of Interest

The authors declare that there is no conflict of interest regarding the publication of this paper.

Funding Statement

The authors have no relevant financial or non-financial interests to disclose.

References

[1] H. Bakhtar *et al.*, "Flow-induced noise and vibration in axial fan: a case study," *Journal of Umm Al-Qura University for Engineering and Architecture,* vol. 15, pp. 1-18, 2024, doi: https://doi.org/10.1007/s43995-024-00079-9.

[2] A. Bouanik, T. Azzam, A. Larabi, A. Mammeri, M. Mekadem, and F. Bakir, "Passive blowing strategy to enhance aerodynamic performance and noise of a hollow-bladed axial fan: An experimental study," *Journal of Applied Fluid Mechanics,* vol. 17, no. 10, pp. 2079-2091, 2024, doi: https://doi.org/10.47176/jafm.17.10.2665.

[3] N. Liu, C. Jiang, L. Huang, and C. Wang, "Effect of porous casing on small axial-flow fan noise," *Applied Acoustics,* vol. 175, p. 107808, 2021, doi: https://doi.org/10.1016/j.apacoust.2020.107808.

[4] M. Yadegari, F. Ommi, S. K. Aliabadi, and Z. Saboohi, "Reducing the aerodynamic noise of the axial flow fan with perforated surface," *Applied Acoustics,* vol. 215, p. 109720, 2024, doi: https://doi.org/10.1016/j.apacoust.2023.109720.

[5] S. Floss, F. Czwielong, S. Becker, and M. Kaltenbacher, "Micro-perforated panels for noise reduction," *Elektrotechnik und Informationstechnik: e & i,* vol. 138, no. 3, pp. 171-178, 2021, doi: https://doi.org/10.1007/s00502-021-00889-y

[6] F. Czwielong, S. Floss, M. Kaltenbacher, and S. Becker, "Influence of a micro-perforated duct absorber on sound emission and performance of axial fans," *Applied Acoustics,* vol. 174, p. 107746, 2021, doi: https://doi.org/10.1016/j.apacoust.2020.107746.

[7] D. L. Sutliff and M. G. Jones, "Low-speed fan noise attenuation from a foam-metal liner," *Journal of aircraft,* vol. 46, no. 4, pp. 1381-1394, 2009, doi: https://doi.org/10.2514/1.41369.

[8] D. L. Sutliff, M. G. Jones, and T. C. Hartley, "High-speed turbofan noise reduction using foam-metal liner over-the-rotor," *Journal of aircraft,* vol. 50, no. 5, pp. 1491-1503, 2013, doi: https://doi.org/10.2514/1.C032021.

[9] B. Dong, D. Xie, F. He, and L. Huang, "Noise attenuation and performance study of a small-sized contra-rotating fan with microperforated casing treatments," *Mechanical Systems and Signal Processing,* vol. 147, p. 107086, 2021, doi: https://doi.org/10.1016/j.ymssp.2020.107086.

[10] D. Sun, J. Li, X. Dong, R. Xu, and X. Sun, "Foam-metal casing treatment on an axial flow compressor: Stability improvement and noise reduction," *Journal of Turbomachinery,* vol. 144, no. 1, p. 011003, 2022, doi: https://doi.org/10.1115/1.4051782.

[11] D. Sun, J. Li, R. Xu, X. Dong, D. Zhao, and X. Sun, "Effects of the foam metal casing treatment on aerodynamic stability and aerocoustic noise in an axial flow compressor," *Aerospace Science and Technology,* vol. 115, p. 106793, 2021, doi: https://doi.org/10.1016/j.ast.2021.106793.

[12] T. Lu, C. Liu, N. Wang, C. Shao, and Y. Li, "Ultra-broadband acoustic metaliner for fan noise reduction," *International Journal of Mechanical Sciences,* vol. 293, p. 110173, 2025, doi: https://doi.org/10.1016/j.ijmecsci.2025.110173.

[13] B. Kenchappa and K. Shivakumar, "Evaluation of a microporous acoustic liner using advanced noise control fan engine," *Applied Sciences,* vol. 15, no. 9, p. 4734, 2025, doi: https://doi.org/10.3390/app15094734.

[14] W.-Q. Wu, Y.-B. Zhang, L. Xu, L.-X. Zhao, and T.-G. Chen, "Design and evaluation of an acoustic metamaterial for ducted fan noise control," *Applied Acoustics,* vol. 233, p. 110612, 2025, doi: https://doi.org/10.1016/j.apacoust.2025.110612.

[15] K. Yeranee and Y. Rao, "A review of recent investigations on flow and heat transfer enhancement in cooling channels embedded with triply periodic minimal surfaces (TPMS)," *Energies,* vol. 15, no. 23, p. 8994, 2022, doi: https://doi.org/10.3390/en15238994.

[16] D. Svoboda, P. Berkova, F. Vlach, D. Beckovsky, M. Gabzdyl, and M. Deutsch, "Noise reduction of air distribution grilles using 3D printed infill structures," *Journal Akustika,* vol. 45, no. 45, 03/31 2023, doi: https://doi.org/10.36336/akustika2023453.

[17] W. Yang, J. An, C. K. Chua, and K. Zhou, "Acoustic absorptions of multifunctional polymeric cellular structures based on triply periodic minimal surfaces fabricated by stereolithography," *Virtual and Physical Prototyping,* vol. 15, no. 2, pp. 242-249, 2020, doi: https://doi.org/10.1080/17452759.2020.1740747.

[18] G. Chouhan, P. Bidare, and G. Bala Murali, "Triply periodic minimal surface based lattices for acoustic performance," *Noise & Vibration Worldwide,* vol. 55, no. 8, pp. 454-468, 2024, doi: https://doi.org/10.1177/09574565241270201.

[19] H. Xiao, H. Dai, N. Dai, and L. Zhou, "Simultaneous acoustic and vibration isolation metamaterials based on triply periodic minimal surface," *Thin-Walled Structures,* vol. 207, p. 112738, 2025, doi: https://doi.org/10.1016/j.tws.2024.112738.

[20] M. Mozafari, M. Masdari, Q. Zhang, and M. Tahani, "Aeroacoustic impact of triply periodic minimal surface porous casings on axial flow fans," *Physics of Fluids,* vol. 37, no. 1, 2025, doi: https://doi.org/10.1063/5.0248030.

[21] R. Dewangan and N. Kumar, "Triply periodic minimal surface (TPMS) metamaterial exhibiting simultaneously superior acoustic and mechanical energy absorption performance," in *ISME International Conference on Advances in Mechanical Engineering*, 2023: Springer, pp. 85-97, doi: https://doi.org/10.1007/978-981-97-3651-5_8.

[22] E. Maevskaia, J. Guerrero, C. Ghayor, I. Bhattacharya, and F. E. Weber, "Triply periodic minimal surface-based scaffolds for bone tissue engineering: A mechanical, in vitro and in vivo study," *Tissue Engineering Part A,* vol. 29, no. 19-20, pp. 507-517, 2023.

[23] Y. Zhang *et al.*, "Adaptive enhancement design of triply periodic minimal surface lattice structure based on non-uniform stress distribution," *Applied Mathematics and Mechanics,* vol. 44, no. 8, pp. 1317-1330, 2023, doi: https://doi.org/10.1007/s10483-023-3013-9.

[24] L. Bowen, A. Celik, M. Westin, and M. Azarpeyvand, "The role of porous structure on airfoil turbulence interaction noise reduction," *Physics of Fluids,* vol. 36, no. 2, 2024, doi: https://doi.org/10.1063/5.0186501.

[25] C. Laloglu and R. Deiterding, "Simulation of the flow around an oscillating cylinder with adaptive lattice Boltzmann methods," in *In Proceedings of the Fifth International Conference on Parallel, Distributed, Grid and Cloud Computing for Engineering*, 2017: Civil-Comp Press, p. 15, doi: https://doi.org/10.4203/ccp.111.19.

[26] F. Ducros, F. Nicoud, and T. Poinsot, "Wall-adapting local eddy-viscosity models for simulations in complex geometries," *Numerical Methods for Fluid Dynamics VI,* vol. 6, pp. 293-299, 1998.

[27] R. Brionnaud, M. Chávez Modena, G. Trapani, and D. M. Holman, "Direct noise computation with a Lattice-Boltzmann method and application to industrial test cases," in *22nd AIAA/CEAS aeroacoustics conference*, 2016, p. 2969, doi: https://doi.org/10.2514/6.2016-2969.

[28] E. Antoniou, G. Romani, A. Jantzen, F. Czwielong, and S. Schoder, "Numerical flow noise simulation of an axial fan with a Lattice-Boltzmann solver," *Acta Acustica,* vol. 7, p. 65, 2023, doi: https://doi.org/10.1051/aacus/2023060

[29] D. Ghodake, M. Sanjosé, S. Moreau, and M. Henner, "Effect of sweep on axial fan noise sources using the lattice Boltzmann method," *International Journal of Turbomachinery, Propulsion and Power,* vol. 7, no. 4, p. 34, 2022, doi: https://doi.org/10.3390/ijtpp7040034.

[30] K. Nagendra and D. K. Tafti, "Flows through reconstructed porous media using immersed boundary methods," *Journal of Fluids Engineering,* vol. 136, no. 4, p. 040908, 2014, doi: https://doi.org/10.1115/1.4026102.

[31] S. Thibault, D. Holman, S. Garcia, and G. Trapani, "CFD Simulation of a quad-rotor UAV with rotors in motion explicitly modeled using an LBM approach with adaptive refinement," in *55th AIAA aerospace sciences meeting*, 2017: American Institute of Aeronautics and Astronautics, p. 0583, doi: https://doi.org/10.2514/6.2017-0583.